

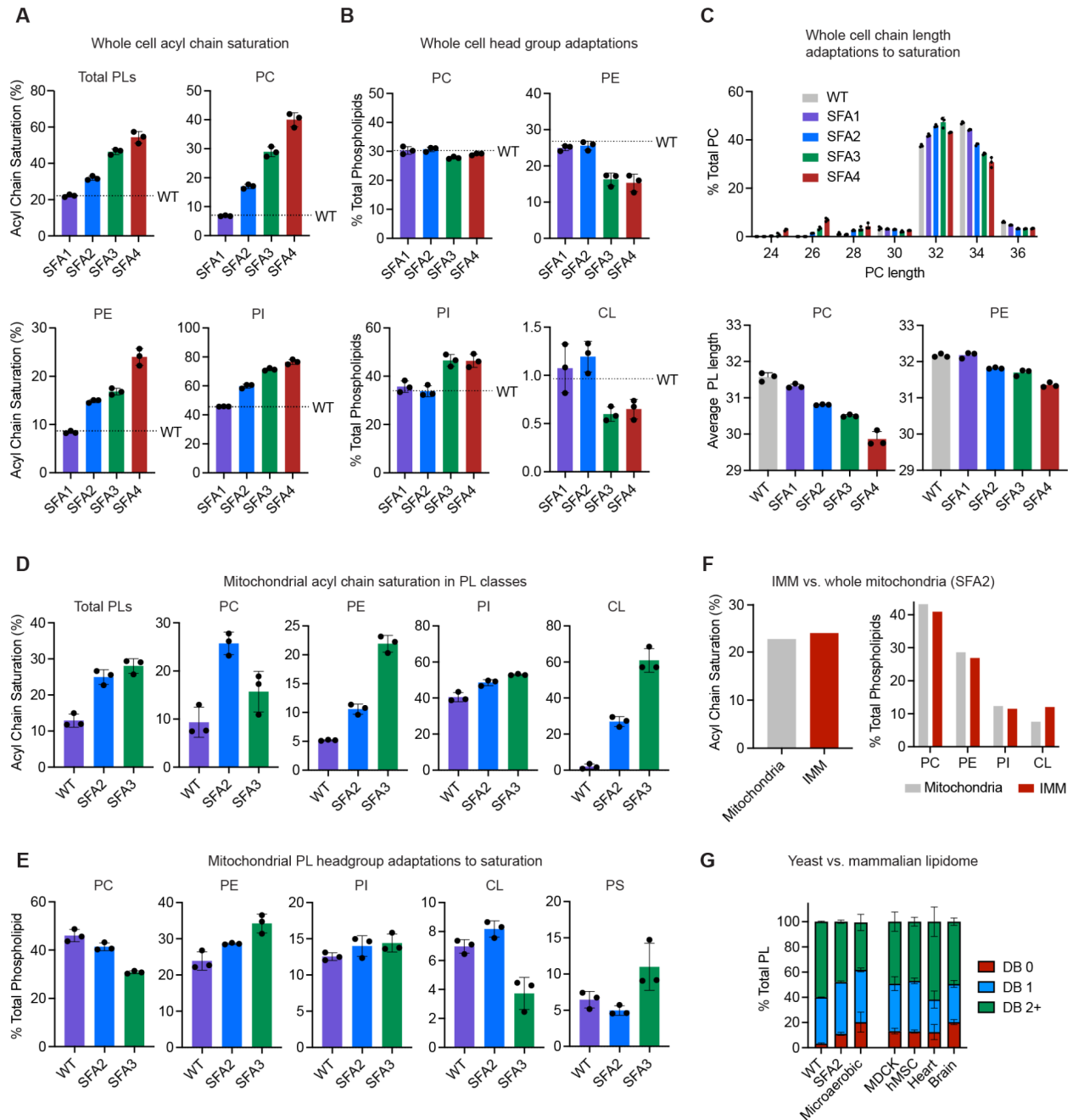
Appendix

Cristae formation is a mechanical buckling event controlled by the inner membrane lipidome

Kailash Venkatraman, Christopher T. Lee, Guadalupe C. Garcia, Arijit Mahapatra, Daniel Milshteyn, Guy Perkins, Keun-Young Kim, H. Amalia Pasolli, Sebastien Phan, Jennifer Lippincott-Schwartz, Mark Ellisman, Padmini Rangamani, and Itay Budin

Contents:

| | |
|-----------------------|-------------|
| Appendix Figures S1-7 | Pages 2-9 |
| Appendix Tables S1-5 | Pages 10-13 |
| Modeling Procedures | Pages 14-20 |
| References | Pages 21-24 |



Appendix Figure S1: Changes to whole cell and mitochondrial lipid profile upon modulation of Ole1p expression.

(A) Decreasing Ole1p expression increases the acyl chain saturation of the total yeast PL pool, and major PL classes as assayed by lipidomics, error bars indicate SD, n=3 independent cultures. WT levels are shown as dotted lines.

(B) Potentially compensatory changes to the whole cell lipidome in response to increasing saturation. Shown are the abundance of major yeast PLs in SFA strains, n=3 independent cultures. WT levels shown as dotted lines. As saturation increases, PE and CL decrease, while PI increases. Error bars indicate SD.

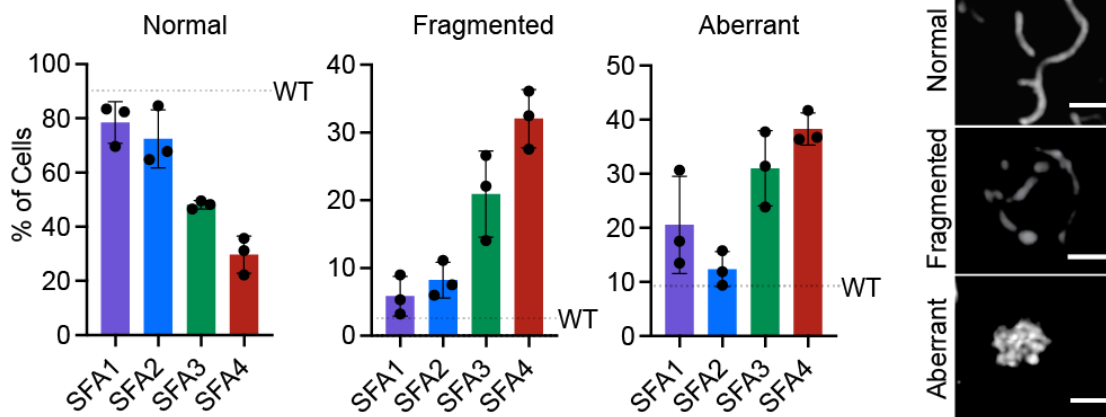
(C) Increasing lipid saturation results in shortening of PC and PE acyl chains in the whole cell. Shown are the sum of the lengths for the *sn-1* and *sn-2* chains.

(D) Acyl chain saturation in isolated mitochondria from SFA strains and WT as determined by intact lipid analysis for the total PL pool, n=3 independent cultures. Error bars indicate SD.

(E) PL headgroup adaptations in isolated mitochondria from SFA strains and wild-type in major PL classes as determined by lipidomic analysis, n=3 independent cultures. In the mitochondria, PC decreases and PE increases as saturation increases. Error bars indicate SD.

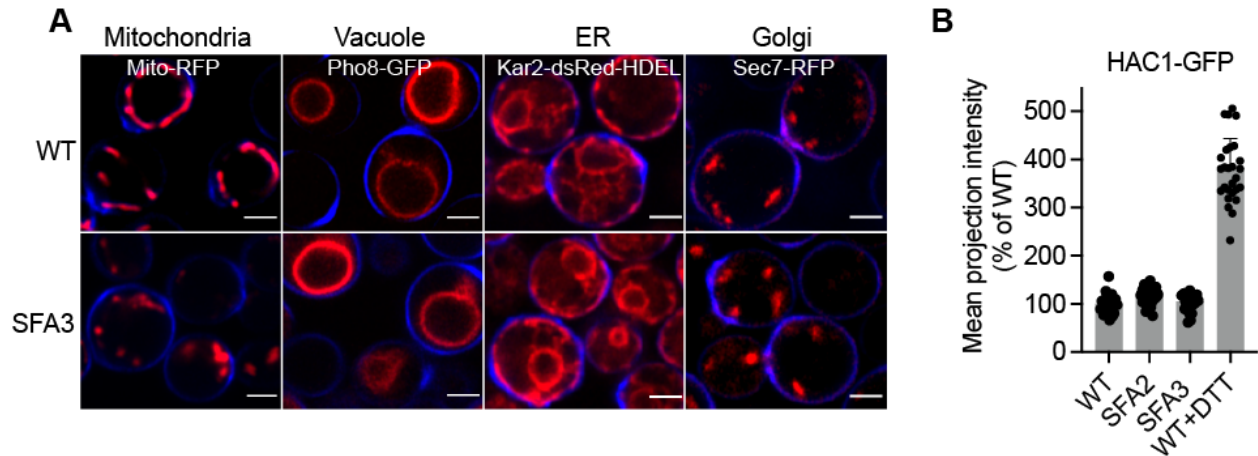
(F) The IMM and whole mitochondrial lipidome display similar levels of saturation and PE/PC, but differ in abundance of CL (higher in the IMM).

(G) Mammalian lipidomes contain similar lipid saturation profiles to yeast SFA2 and micro-aerobically grown cells, where CL is essential. Shown is the double bond profile of all PLs as determined through lipidomics from *S. cerevisiae* (this study) in comparison with mammalian cell lines (MDCK-CM and hMSC-CM) and isolated tissues previously analyzed using the same lipidomics platform (Symons *et al*, 2021). WT yeast grown under vigorous aeration have a low number of saturated and monounsaturated PLs, while WT cells grown under physiologically-relevant oxygen concentrations (microaerobic) or engineered strains (SFA2) show profiles more similar to mammalian cells. In the latter systems, CL is an essential component for proper mitochondrial biogenesis. Error bars indicate SD.



Appendix Figure S2: Pipeline for quantifying changes in mitochondrial morphology observed in SFA strains.

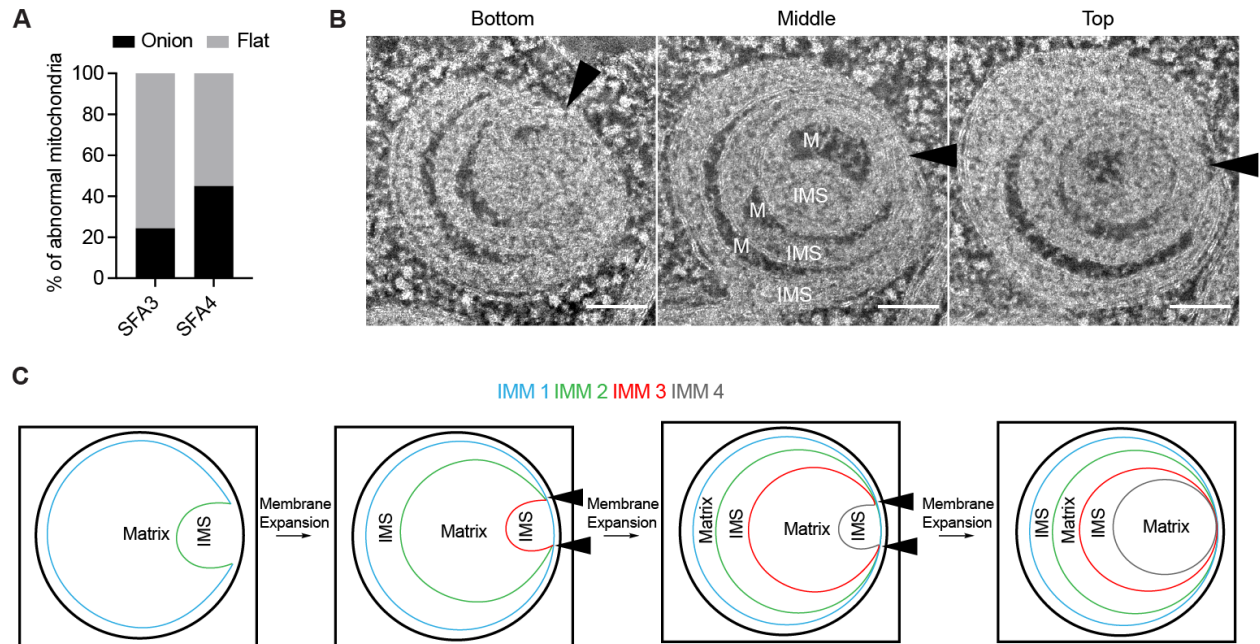
Imaging of matrix-localized RFP was used to quantify the frequency of mitochondrial abnormality as a function of the amounts of normal, fragmented and aberrant mitochondria. Normal mitochondria contain tubulations throughout the whole yeast cell, while fragmented mitochondria retain an overall mitochondrial structure but have lost the interconnected tubular network associated with normal mitochondria. Aberrant mitochondria are characterized by punctate aggregations of mitochondria in the center of the yeast cell. Cells were imaged in n=3 independent cultures. Error bars indicate SD. Scale bars, 2 μm.



Appendix Figure S3: PL saturation causes defects to mitochondrial morphology while other organelles remain intact.

(A) Decreasing expression of Ole1p expression results in abnormal mitochondria in SFA3 while other organelles remain intact. Organelles were imaged in cells that were transformed with plasmids expressing the following fusion proteins: mts-RFP (Mitochondria), Pho8-GFP (Vacuole), Kar2-dsRed-HDEL (ER), Sec7-RFP (Golgi). Cells were grown to exponential phase and were stained with cell wall-binding calcofluor white (blue). Scale bars, 2 μ m.

(B) ER stress was measured through induction of the unfolded protein response (UPR) using a HAC1-GFP splice reporter as previously described. GFP intensity was quantified in 3D projections from N=20 cells; the transition between SFA2/3 did not show any increase in UPR activation. WT cells treated with 2 mM dithiothreitol (DTT) were used as a positive control. Error bars indicate SD.

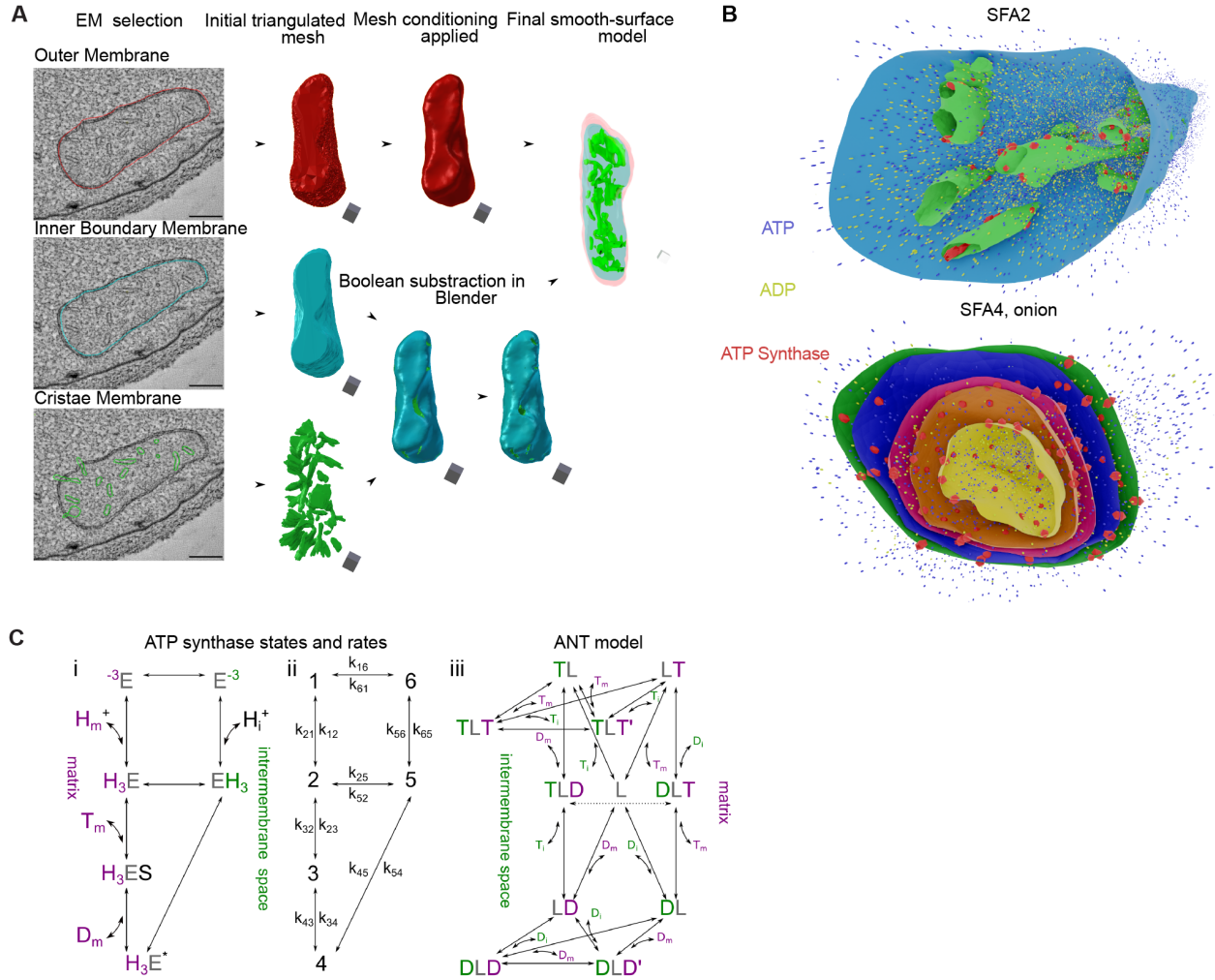


Appendix Figure S4: Multi-tilt electron tomography reveals a mechanism for onion-formation in aberrant mitochondria.

(A) Quantitative analysis of thin-section TEM micrographs reveals the abnormal mitochondria in SFA3 are predominantly flat, while in SFA4 there is an even distribution of onion and flat abnormal mitochondria. At least N=40 mitochondria were quantified from each strain.

(B) Multi-tilt tomogram slices of HPFS SFA4 yeast cells at three z-positions. 'M' indicates matrix regions (dark), while 'IMS' indicates intermembrane space regions (light). Shading indicates alternating matrix and IMS regions, as previously observed (Paumard *et al*, 2002). Black triangles indicate observed regions of contact points between IMM layers, suggesting a continuous IMM. Scale bars, 100 nm.

(C) Schematic depiction for one model of how onion-like morphology could be formed by a continuous IMM undergoing subsequent buddings during its biogenesis due to membrane expansion. Black triangles indicate regions of contact points between multiple apparent IMM layers that are continuous.

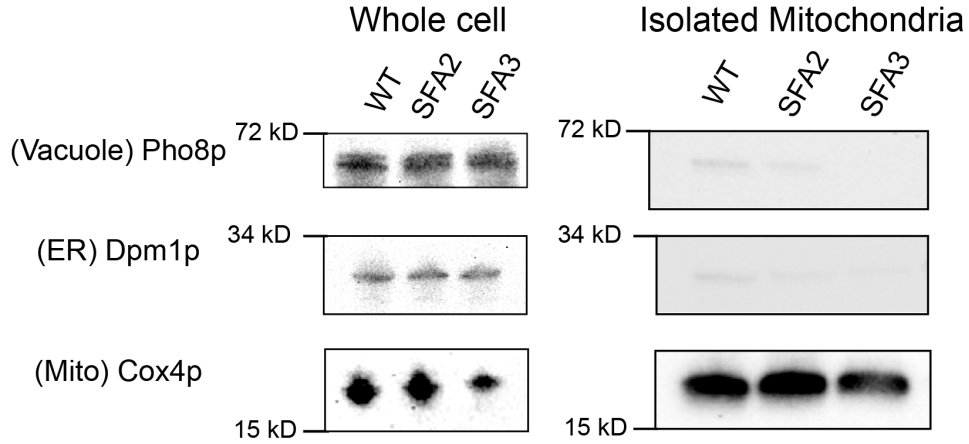


Appendix Figure S5: Pipeline for mesh generation from multi-tilt tomography for ATP synthesis simulations.

(A) Example of Blender-based 3D Mesh generation pipeline from EM tomograms.

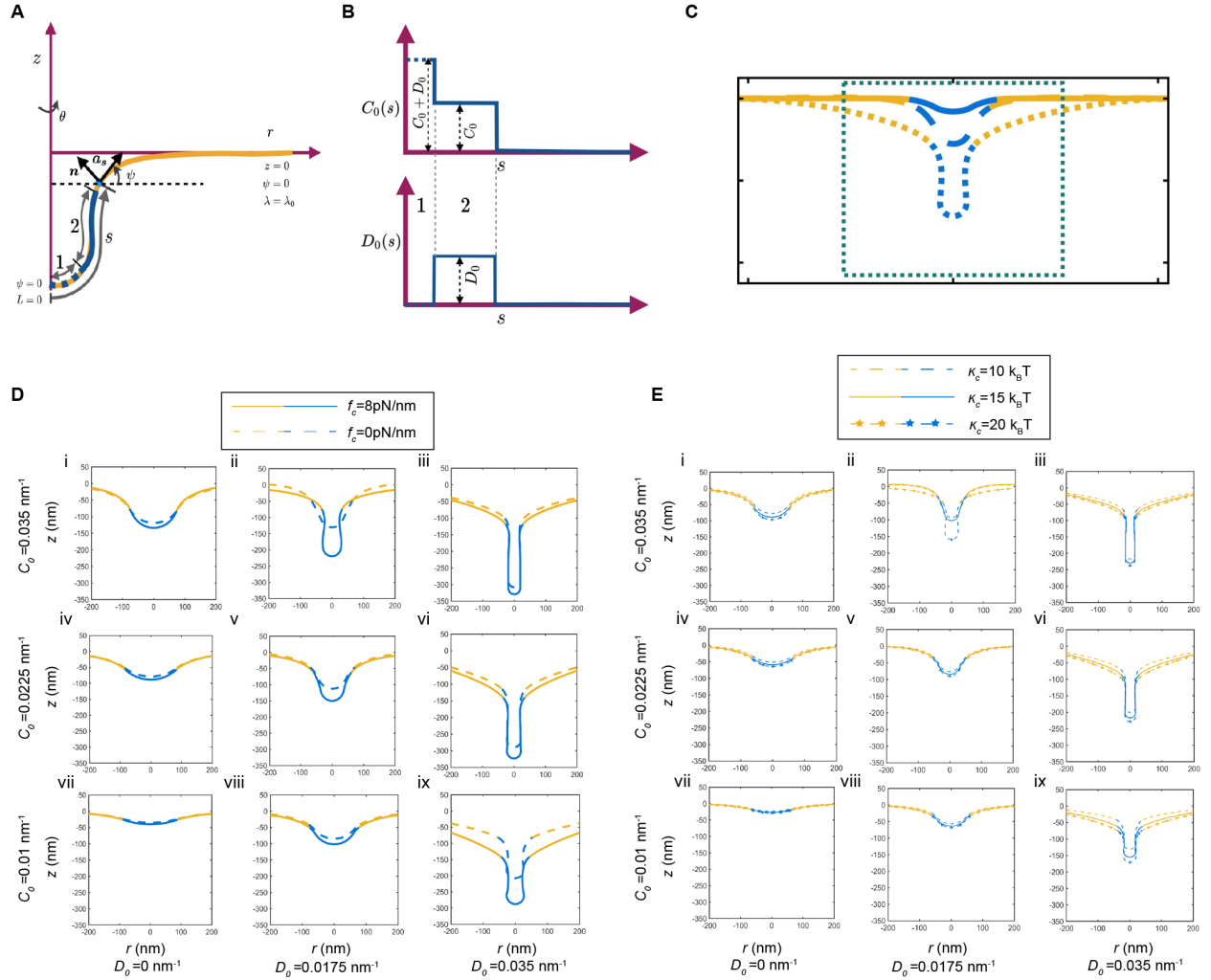
(B) Snapshots of ATP generation simulations as displayed in Movie S4 and S5. SFA2 shows localizations of ATP synthases to regions of high curvature in CMs, while in the SFA4 onion ATP synthases are distributed evenly on each layer of IMM based on previous cryo electron tomography reconstructions.

(C) (i-iii) Schematic representations of the kinetic states and modeled rates of ATP synthase and ANT used to construct the metabolic model. Further details of the model can be found in the appendix modeling procedures.



Appendix Figure S6: Isolated mitochondrial fractions are bereft of contamination from other organelles.

Whole cell lysates were first grown to the stationary phase in YPEG. 2.5 OD units of cells were taken and subjected to protein extraction and SDS-PAGE as previously described (Kushnirov, 2000). Gels were then transferred and western blotted before decoration with antibodies against the vacuole, ER and mitochondria. For isolated mitochondria, 10 μ g of protein was loaded and subjected to western blotting against organelle antibodies. For each antibody, the following dilutions were used: 1:1000 for Cox4p and Dpm1p and 1:250 for Pho8p.



Appendix Figure S7: Continuum modeling details and comparison of tubular morphologies with and without an applied collar force.

(A) Schematic showing the axisymmetric membrane configuration along with the boundary conditions. The yellow regions depict the bare lipid bilayer, and the blue regions depict the regions where different spontaneous curvatures are prescribed.

(B) Prescription of isotropic and anisotropic spontaneous curvature along the arc length in the simulations.

(C) The simulation domain is large to avoid boundary effects but the zoomed in portion in the dashed box is shown to demonstrate the shapes of the membrane.

(D) Comparison of the tubular shapes with (solid lines) and without (dashed line) the collar force at the base of the cristae. All parameters are the same as those in Figure 5B. Presence of a collar force promoted cristae like structures for the same values of imposed curvatures. This is particularly apparent in panel ii.

(E) Shapes of the membrane for the same values of coat area, collar force, and variations in the isotropic and anisotropic spontaneous curvature as panel D for different values of bending modulus. We observe that the shapes of the tubular cristae are not sensitive to changes in bending modulus for low curvature values but differences in membrane curvature can be seen for high values of isotropic and anisotropic spontaneous curvatures.

Supplementary Tables

Appendix Table S1A: Bending moduli (κ_c) values extracted from X-ray scattering analysis or micropipette aspiration analysis of PC membranes as a function of acyl chain saturation.

X-ray scattering

| Lipid | Acyl Chains | κ_c (10^{-20} J) | Source |
|-------|-------------|----------------------------|-------------------------------|
| POPC | 16:0 18:1 | 8.5 | (Kucerka <i>et al</i> , 2005) |
| DOPC | 18:1 18:1 | 8.5±0.6 | (Jablin <i>et al</i> , 2014) |

Micropipette aspiration

| Lipid | Acyl Chains | κ_c (10^{-19} J) | Source |
|-------|-------------|----------------------------|------------------------------|
| SOPC | 18:0 18:1 | 0.90±0.06 | (Rawicz <i>et al</i> , 2000) |
| DOPC | 18:1 18:1 | 0.85±0.10 | (Rawicz <i>et al</i> , 2000) |

Appendix Table S1B: Bending moduli (κ_c) values extracted from MD simulations of PE as a function of acyl chain saturation.

| Lipid | Acyl Chains | κ_c (10^{-20} J) | Source |
|-------|-------------|----------------------------|-------------------------------|
| POPE | 16:0 18:1 | 13.3±0.6 | (Venable <i>et al</i> , 2015) |
| DOPE | 18:1 18:1 | 11.8±0.3 | (Venable <i>et al</i> , 2015) |

Appendix Table S1C: Spontaneous curvature (c_0) values extracted from SAXS analysis of PC and PE lipids as a function of acyl chain saturation.

PC

| Lipid | Acyl Chains | Matrix | c_0 (nm^{-1}) | Source |
|-------|-------------|--------|----------------------------|-----------------------------------|
| DPPC | 16:0 16:0 | DOPE | 0.05±0.05 | (Kaltenegger <i>et al</i> , 2021) |
| POPC | 16:0 18:1 | DOPE | 0.01±0.04 | (Kaltenegger <i>et al</i> , 2021) |
| DOPC | 18:1 18:1 | DOPE | -0.04±0.04 | (Kaltenegger <i>et al</i> , 2021) |

PE

| Lipid | Acyl Chains | Matrix | c_0 (nm^{-1}) | Source |
|-------|-------------|--------|----------------------------|-------------------------------|
| POPE | 16:0 18:1 | - | -0.317±0.007 | (Frewein <i>et al</i> , 2019) |

| | | | | |
|--------|-----------|---|--------------|-------------------------------|
| DiPoPE | 16:1 16:1 | - | -0.382±0.009 | (Frewein <i>et al</i> , 2019) |
| DOPE | 18:1 18:1 | - | -0.409±0.010 | (Frewein <i>et al</i> , 2019) |

Appendix Table S2: List of membrane compositions simulated by CG-MD; the number of lipids for each type are shown.

| System name | POPC | DOPC | POPE | DOPE | CDL1 | CDL2 | POPG | DOPG |
|------------------------------|------|------|------|------|------|------|------|------|
| 1: Complex WT (CL-1) | 648 | 2486 | 162 | 1460 | 648 | 0 | 0 | 0 |
| 2: Complex SFA2 (CL-1) | 1406 | 1352 | 432 | 1568 | 648 | 0 | 0 | 0 |
| 3: Complex SFA3 (CL-1) | 972 | 1406 | 1188 | 1188 | 648 | 0 | 0 | 0 |
| 4: Complex WT (CL-2) | 648 | 2486 | 162 | 1460 | 0 | 648 | 0 | 0 |
| 5: Complex SFA2 (CL-2) | 1406 | 1352 | 432 | 1568 | 0 | 648 | 0 | 0 |
| 6: Complex SFA3 (CL-2) | 972 | 1406 | 1188 | 1188 | 0 | 648 | 0 | 0 |
| 7: Complex WT (PG) | 540 | 2974 | 108 | 1188 | 0 | 0 | 324 | 270 |
| 8: Complex SFA2 (PG) | 1080 | 1838 | 378 | 1352 | 0 | 0 | 648 | 108 |
| 9: Complex SFA3 (PG) | 918 | 1406 | 1188 | 1134 | 0 | 0 | 648 | 108 |
| 10: Ideal DOPL (CL-1) | 0 | 2704 | 0 | 1622 | 1080 | 0 | 0 | 0 |
| 11: Ideal POPL (CL-1) | 2704 | 0 | 1622 | 0 | 1080 | 0 | 0 | 0 |
| 12: Ideal DOPL (CL-2) | 0 | 2704 | 0 | 1622 | 0 | 1080 | 0 | 0 |
| 13: Ideal POPL (CL-2) | 2704 | 0 | 1622 | 0 | 0 | 1080 | 0 | 0 |
| 14: Ideal DOPL (PG) | 0 | 2704 | 0 | 1622 | 0 | 0 | 0 | 1080 |
| 15: Ideal POPL (PG) | 2704 | 0 | 1622 | 0 | 0 | 0 | 0 | 1080 |
| 16: Outer IMM leaflet (CL-1) | 594 | 2378 | 162 | 1406 | 864 | 0 | 0 | 0 |
| 17: Inner IMM leaflet (CL-1) | 648 | 2594 | 162 | 1514 | 486 | 0 | 0 | 0 |
| 18: Outer IMM leaflet (CL-2) | 594 | 2378 | 162 | 1406 | 0 | 864 | 0 | 0 |
| 19: Inner IMM leaflet (CL-2) | 648 | 2594 | 162 | 1514 | 0 | 486 | 0 | 0 |
| 20: Pure CL-1 | 0 | 0 | 0 | 0 | 5408 | 0 | 0 | 0 |
| 21: Pure CL-2 | 0 | 0 | 0 | 0 | 0 | 5408 | 0 | 0 |

Appendix Table S3: Strains used in this study

Experimental Models: Organisms/strains

| Reagent or Resource | Source | Description |
|--|------------|---|
| W303a (<i>MATa leu2-3112 trp1-1 can1-100 ura3-1 ade2-1 his3-11,15</i>) | ATCC | Haploid background strain |
| W303a, <i>ole1::Pm1-OLE1</i> | This study | Weak constitutive promoter driving <i>OLE1</i> expression (SFA4) |
| W303a, <i>ole1::Pm2-OLE1</i> | This study | Weak constitutive promoter driving <i>OLE1</i> expression (SFA3) |
| W303a, <i>ole1::Pm3-OLE1</i> | This study | Medium strength constitutive promoter driving <i>OLE1</i> expression (SFA2) |
| W303a, <i>ole1::Pm4-OLE1</i> | This study | Strong constitutive promoter driving <i>OLE1</i> expression (SFA1) |
| W303a, <i>ole1::Pm1-OLE1 crd1Δ::KanMX6</i> | This study | SFA4 <i>crd1Δ</i> |
| W303a, <i>ole1::Pm2-OLE1 crd1Δ::KanMX6</i> | This study | SFA3 <i>crd1Δ</i> |
| W303a, <i>ole1::Pm3-OLE1 crd1Δ::KanMX6</i> | This study | SFA2 <i>crd1Δ</i> |
| W303a, <i>ole1::Pm4-OLE1 crd1Δ::KanMX6</i> | This study | SFA1 <i>crd1Δ</i> |
| W303a, <i>crd1Δ::KanMX6</i> | This study | |
| W303a, <i>atp20Δ::His3</i> | This study | |
| W303a, <i>ole1::Pm4-OLE1 atp20Δ::His3</i> | This study | SFA1 <i>atp20Δ</i> |
| W303a, <i>ole1::Pm3-OLE1 atp20Δ::His3</i> | This study | SFA2 <i>atp20Δ</i> |
| W303a, <i>mgm1Δ::His3</i> | This study | |
| W303a, <i>mic60Δ::His3</i> | This study | |
| W303a, <i>ole1::Pm4-OLE1 mic60Δ::His3</i> | This study | SFA1 <i>mic60Δ</i> |
| W303a, <i>ole1::Pm3-OLE1 mic60Δ::His3</i> | This study | SFA2 <i>mic60Δ</i> |
| W303a, <i>atp20Δ::His3, crd1Δ::KanMX6</i> | This study | |

Appendix Table S4: Plasmids used in this study

| Plasmid | Source | Description |
|---------|--------|-------------|
|---------|--------|-------------|

| | | |
|-----------|------------------|----------------------------------|
| pPW1882 | Dr. Peter Walter | Mitochondrial matrix RFP |
| pPW1409 | Dr. Peter Walter | ER-localized RFP |
| pRS416 | Dr. Arnold Seo | Vacuole Pho8 GFP |
| pSEC7-RFP | Dr. Arnold Seo | Early Golgi-RFP |
| Cox4-GFP | Dr. Zhiping Xie | CIV subunit 4-GFP, IMM localized |
| pPW599 | Dr. Peter Walter | UPR splice reporter |

Appendix Table S5: Antibodies used in this study

| Reagent or Resource | Source | Description |
|--|-------------------------|--|
| Anti-ATP synthase subunit β antibody | Dr. Alexander Tzagoloff | Goat anti-rabbit, polyclonal (Rak & Tzagoloff, 2009) |
| Anti-Mic60p | Dr. Andreas Reichart | Goat anti-rabbit (Rabl <i>et al</i> , 2009) |
| Anti-Mgm1p | Dr. Andreas Reichart | Goat anti-rabbit (Rabl <i>et al</i> , 2009) |
| Anti-Cox4p | Abcam | Cat: 110272 |
| Anti-Dpm1p | Abcam | Cat: 113686 |
| Anti-Pho8 | Abcam | Cat: 113688 |
| Anti-Cox1 | Abcam | Cat: 11D8B7 |
| Anti-CRLS1 | Proteintech | Cat: 14845-1-AP |
| Anti-Actin | Invitrogen | Cat: PA5-78715 |

Modeling Procedures

ATP production modeling

The computational for ATP generation in mitochondria is based on previous modeling efforts (Garcia *et al*, 2019, 2022; Magnus & Keizer, 1997; Bertram *et al*, 2006; Saa & Siqueira, 2013). We solve the reactions (detailed below) using MCell (Kerr *et al*, 2008) to accurately capture the stochastic nature of the events underlying ATP production in the small volumes of the mitochondria. The model has a total of 19 equations and 41 parameters and the thermodynamic details are given in (Garcia *et al*, 2022). We briefly describe the main components of the model below.

ATP synthase: The ATP synthase model is composed of ATP synthase (represented as E) that can be in six states (Figure S3F), representing different protein configurations. Each state corresponds with a number from 1 to 6, and each transition has associated a rate constant k_{ij} (transition from the state $i \rightarrow j$). In some cases k_{ij} depends on the membrane potential, proton concentration, or phosphate concentration. The list of reactions and model parameters are given below, reproduced from (Garcia *et al*, 2022). The model was adapted from the work of Pietrobon and Caplan (Pietrobon & Caplan, 1985).

ATP synthase is modeled as a membrane protein that can transport protons (H^+) from and to the matrix and synthesize ATP. The translocation of 3 H^+ is coupled to the phosphorylation of one ADP into ATP, approximating the stoichiometry of the yeast ATP synthase with a c_{10} ring (10 H^+ / 3 ATP). The free enzyme with its negative charged cavity facing the IMS is represented by E^{-3} . Three protons can bind, generating the transition to state EH_3 . The protons can be translocated to the matrix through the reaction ($EH_3 \rightarrow H_3E$) or $EH_3 \rightarrow H_3E^*$. A transition to state H_3ES can follow binding one ADP molecule from the matrix (represented as D_m) under constant phosphate (P_i) concentration, which is kept at 20 mM. This is followed by the production of one molecule of ATP (T_m) through the reaction $H_3ES \rightarrow H_3E + T_m$. Finally, in the transition $H^3E \rightarrow {}^{-3}E + 3H^+_m$ three protons are unbound in the matrix. The negative charged cavity of the enzyme can also transition from facing the matrix (state ${}^{-3}E$) to facing the IMS (state E^{-3}).

Transition $6 \rightarrow 5$ accounts for the binding of 3 protons from the IMS to the free enzyme (state 6, E^{-3}), two transitions can occur from here: transition $5 \rightarrow 4$ represents the transport of the protons to the matrix or transition $5 \rightarrow 2$ that represents the transport of the protons to the matrix without producing ATP. In state 4, ADP can bind to the enzyme (transition $4 \rightarrow 3$) and subsequently ATP can be synthesized (transition $3 \rightarrow 2$). This is followed by the unbinding of the protons in the matrix (transition $2 \rightarrow 1$), arriving at state 1.

List of Reactions for the ATP synthase model: (1) ${}^{-3}E + 3H^+_m \leftrightarrow H_3E$, k_{12} , k_{21} (2) $H_3E + T_m \leftrightarrow H_3ES$, k_{23} , k_{32} (3) $H_3ES \leftrightarrow H_3E^* + D_m$, k_{34} , k_{43} (4) $H_3E^* \leftrightarrow EH_3$, k_{45} , k_{54} (5) $EH_3 \leftrightarrow E^{-3} + H^+_i$, k_{56} , k_{65} (6) $E^{-3} \leftrightarrow {}^{-3}E$, k_{61} , k_{16}

Parameter values for the ATP synthase model: $k_{43} = 2 \times 10^6 \text{ M}^{-1} \text{ s}^{-1}$, $k_{34} = 100 \text{ s}^{-1}$, $k_{12} = 25 \text{ s}^{-1}$, $k_{21} = 40 \text{ s}^{-1}$, $k_{65} = 3969 \text{ s}^{-1}$, $k_{56} = 1000 \text{ s}^{-1}$, $k_{61} = 33989 \text{ s}^{-1}$, $k_{16} = 146516 \text{ s}^{-1}$, $k_{54} = 1 \times 10^2 \text{ s}^{-1}$, $k_{45} = 100 \text{ s}^{-1}$, $k_{25} = 5.85 \times 10^{-30} \text{ s}^{-1}$, $k_{52} = 1 \times 10^{-20} \text{ s}^{-1}$, $k_{32} = 5 \times 10^3 \text{ s}^{-1}$, $k_{23} = 5 \times 10^6 \text{ M}^{-1} \text{ s}^{-1}$

Modeled distribution of ATP synthases: The density of ATP synthases has been estimated at 3070 ATP synthases per μm^2 in areas of high membrane curvature (Acehan *et al*, 2011), this is consistent with ATP synthase densities estimated from yeast (Davies *et al*, 2012). For each reconstruction, we calculated the surface area formed by vertices with first principal curvature

higher than $70 \mu\text{m}^{-1}$, and with this the number of ATP synthases was estimated for each organelle. For instance, the surface area of high curvature for the reconstruction of an SFA2 mitochondria is $0.144 \mu\text{m}^2$, which leads to an estimation of 433 units of ATP synthases in this reconstruction. To perform the spatial simulations, ATP synthases were distributed randomly in the regions of high curvature. For each mitochondrion, the total number of ATP synthases was kept the same.

ATP/ADP translocator (ANT) model: The model for the ATP/ADP translocator (ANT) is composed of 11 states and 22 chemical reactions, listed below. The kinetic diagram is presented in Figure S3F. The free protein is represented with the letter L in the diagram; it can bind ADP (D) or ATP (T) molecules from the matrix side (on the right) or IMS side (on the left), forming a triple molecular state. State TLD for instance represents a state with one ATP bound from the IMS and one ADP from the matrix side. The reaction that transports ATP from the matrix to the IMS is $\text{DLT} \rightarrow \text{TLD}$, the rate constant for this reaction is k_p , the reverse reaction imports ATP to the matrix and exports ADP to the IMS, with rate constant k_{cp} . Futile translocations can also occur translocating one molecule of ATP by another ATP ($\text{TLT} \rightarrow \text{TLT}'$). TLT and TLT' represent the same state, but they are differentiated to measure the rate of these translocations.

List of Reactions for the ANT model: (1) $\text{T}_m + \text{L} \leftrightarrow \text{LT}$, $k_{\text{T}_m}^+$, $k_{\text{T}_m}^-$ (2) $\text{D}_m + \text{L} \leftrightarrow \text{LD}$, $k_{\text{D}_m}^+$, $k_{\text{D}_m}^-$ (3) $\text{T}_i + \text{L} \leftrightarrow \text{TL}$, $k_{\text{T}_i}^+$, $k_{\text{T}_i}^-$ (4) $\text{D}_i + \text{L} \leftrightarrow \text{DL}$, $k_{\text{D}_i}^+$, $k_{\text{D}_i}^-$ (5) $\text{T}_i + \text{LT} \leftrightarrow \text{TLT}$, $k_{\text{T}_i}^+$, $k_{\text{T}_i}^-$ (6) $\text{D}_i + \text{LT} \leftrightarrow \text{DLT}$, $k_{\text{D}_i}^+$, $k_{\text{D}_i}^-$ (7) $\text{T}_i + \text{LD} \leftrightarrow \text{TLD}$, $k_{\text{T}_i}^+$, $k_{\text{T}_i}^-$ (8) $\text{D}_i + \text{LD} \leftrightarrow \text{DLD}$, $k_{\text{D}_i}^+$, $k_{\text{D}_i}^-$ (9) $\text{TLD} \rightarrow \text{DLT}$, k_{cp} (10) $\text{DLT} \rightarrow \text{TLD}$, k_p (11) $\text{TLT} \rightarrow \text{TLT}'$, k_t (12) $\text{TLT}' \rightarrow \text{TLT}$, k_t (13) $\text{DLD} \rightarrow \text{DLD}'$, k_d (14) $\text{DLD} \rightarrow \text{DLD}$, k_d

Parameter values for the ANT model at $\Delta\phi$ 180 mV: $k_{\text{T}_m}^- = 4 \times 10^4 \text{ s}^{-1}$, $k_{\text{T}_m}^+ = 6.4 \times 10^6 \text{ M}^{-1} \text{ s}^{-1}$, $k_{\text{T}_i}^- = 200 \text{ s}^{-1}$, $k_{\text{T}_i}^+ = 4 \times 10^5 \text{ M}^{-1} \text{ s}^{-1}$, $k_{\text{D}_m}^- = 4 \times 10^4 \text{ s}^{-1}$, $k_{\text{D}_m}^+ = 4 \times 10^6 \text{ M}^{-1} \text{ s}^{-1}$, $k_{\text{D}_i}^- = 100 \text{ s}^{-1}$, $k_{\text{D}_i}^+ = 4 \times 10^6 \text{ M}^{-1} \text{ s}^{-1}$, $k_p = 92 \text{ s}^{-1}$, $k_{cp} = 3.5 \text{ s}^{-1}$, $k_d = 4.8 \text{ s}^{-1}$, $k_t = 5.8 \text{ s}^{-1}$

Modeled distribution of ANTs: The density of ANTs has been estimated at 0.2 nm/mg protein in rat liver mitochondria (Forman & Wilson, 1983). Assuming that 1 nm/mg protein is approximately 1.25 mM (Magnus & Keizer, 1997) leads to a concentration of 0.25 mM. With this concentration, the number of ANTs in a given reconstruction can be estimated. Using the total mitochondrial volume proportionality with ANT concentration, we set the number of ANTs in SFA2 as 7678. In the onion mitochondrion, the number of ANTs were set at 7531. Thus, both types of mitochondria analyzed contained a 17:1 ratio of ANTs to ATP synthases.

VDAC model: To model the exit of ATP molecules to the cytosol we included VDACS, the main mechanism for metabolites to cross the OM. We implemented a simple model assuming VDAC proteins interact with ATP molecules and translocate them to the cytosol by the reaction $\text{VDAC} + \text{ATP}_{\text{IMS}} \rightleftharpoons \text{VDAC} + \text{ATP}_{\text{cyto}}$. In all simulations, VDAC proteins were homogeneously distributed in the OMM. VDAC abundances were set as proportional to the total mitochondrial volume encapsulated by the OMM.

Parameters for the VDAC mode: rate constant of the reaction, $k_{\text{vdac}} = 1 \times 10^6 \text{ M}^{-1} \text{ s}^{-1}$, the density of VDACS (De Pinto *et al*, 1987), $\delta = 1 \times 10^4 \mu\text{m}^{-2}$, the number of VDACS considered in the simulations, $N_{\text{vdac}} = 10268$ for CM-containing SFA2 mitochondria and 4979 for onion-like SFA4 mitochondria.

Metabolite buffers: ATP and ADP molecules can interact with different cations, be bound, or ionized. The total concentration of ATP and ADP molecules can be distributed in several compounds like ATP^{4-} , ADP^{3-} , ATPMg^{2-} , etc. The final distributions can be estimated by

coefficients representing the fraction of unbound ATP in the matrix or the IMS. For our model, mitochondrial ADP³⁻ and ATP⁴⁻ concentrations were estimated analogously to published data (Magnus & Keizer, 1997) as $[\text{ADP}]_{\text{m,free}} = 0.8 [\text{ADP}]_{\text{m}}$, $[\text{ATP}]_{\text{m,free}} = [\text{ATP}]_{\text{m}}$, $[\text{ATP}^{4-}] = 0.05 [\text{ATP}]_{\text{free}}$ and $[\text{ADP}^{3-}] = 0.45 [\text{ADP}]_{\text{free}}$. The initial concentrations of ATP and ADP in the matrix were set to 13 mM and 2 mM, respectively, and to 6.5 mM and 0.1 mM in the IMS and cytosol. In some simulations, these concentrations were kept constant.

Well-mixed model of ATP generation: A system of ordinary differential equations was derived from the reactions above (given in (Garcia *et al*, 2022)) and used to calculate the rate of ATP generation in a well-mixed model, without considerations of mitochondrial geometry.

Molecular dynamics simulations

Coarse grained molecular dynamics models of systems with varying compositions were generated using insane.py (Wassenaar *et al*, 2015) and Martini 2.2 force-field parameters (Marrink *et al*, 2007, 2004). Minimization and equilibration followed the conventional protocols established by CHARMM-GUI (Qi *et al*, 2015; Jo *et al*, 2007), summarized briefly here. Initial soft-core minimization is followed by steepest descent to generate an integrator ready relaxed configuration. The systems are jumped to 303 K by random assignment of velocities and the systems undergo several steps of NPT restrained equilibration. All equilibration steps were run with the Berendsen barostat (Berendsen *et al*, 1984). Over the course of restrained equilibration stages, the timestep was gradually increased from 2 to 20 fs, and bilayer headgroup restraints were reduced from 200 to 20 KJ/mol nm². Systems are followed by several microseconds of NPT production using a semiisotropic Parinello-Rahman barostat (Parinello & Rahman, 1981). All equilibration and production simulations use the Bussi-Donadio-Parinello velocity-rescaling thermostat (Bussi *et al*, 2007) with reaction-field electrostatics and shifted Van der Waals potentials both with 1.1 nm cutoff (de Jong *et al*, 2016). Molecular dynamics simulations were run using gromacs 2022.1 (Bauer *et al*, 2022; Abraham *et al*, 2015). Force-field parameters, topologies, and simulation control parameters to reproduce this work are available <https://github.com/RangamaniLabUCSD/2022-mitochondria-lipidomics-md>. Henceforth all timescales reported are in simulation time, and not scaled using the conventional factor of 4 for Martini 2.2 simulations.

The bending modulus of the membrane for each composition was estimated by analyzing the height fluctuation spectra (Brown, 2008; Venable *et al*, 2015; Helfrich, 1973; Ergüder & Deserno, 2021; Fowler *et al*, 2016) of systems approximately 40 by 40 nm in size over 5 μ s of production. Assuming the Helfrich Hamiltonian in the limit of small deformations (Monge gauge), zero membrane tension, and equipartition of energy, the power spectrum of the bilayer height fluctuations is given by,

$$\langle |h(\mathbf{q})|^2 \rangle = \frac{k_B T}{L^2 K_c q^4},$$

Where q is the magnitude of wave-vector \mathbf{q} , $k_B T$ is the Boltzmann constant and temperature, L is the system length, and K_c is the membrane bending modulus. Quadrilateral meshes representing the surfaces of each leaflet are fit to the headgroup region (defined by the pointcloud of PO4 and GL0 beads) using piecewise cubic interpolation. The neutral surface of the bilayer was assumed to be the mean of the two surfaces. Computing the squared discrete fourier transform of the neutral surface, we obtained the 2D power spectrum of height fluctuations. The 2D power spectrum was converted into 1D for subsequent analysis by radially binning and averaging. Fitting the 1D power spectrum to the theoretical enables the estimation of the membrane bending modulus. Quantifying the error of the estimate is performed using

parametric bootstrapping analysis following recommendations by Erguder and Deserno (Ergüder & Deserno, 2021). In brief, we have a sequence of mean squared amplitudes, $\langle |h(\mathbf{q})|^2 \rangle$ for each q corresponding to each trajectory frame. To obtain a meaningful error we consider these as samples from a continuous trajectory with some potential correlation. Statistical block averaging enables us to estimate the autocorrelation time of the data and further a correlation corrected standard deviation. The standard error of the bending modulus is determined from using parametric bootstrapping to sample values of spectral power for large wavenumbers. These are subject to a non-linear fit to obtain a distribution of K_c values for each system from which we obtain the standard deviation. Processing of the data for the analysis was performed using numpy (Harris *et al*, 2020), Scipy (Virtanen *et al*, 2020), MDAnalysis (Virtanen *et al*, 2020), and a modified curvature analysis framework (E., 2021) available from <https://github.com/ctlee/membrane-curvature>.

The local neighbor enrichment for each lipid type was investigated using MDAnalysis (Virtanen *et al*, 2020). For each lipid, we count the numbers and types of each lipid within a 1.5 nm radius. The position of each lipid was either the sole PO4 or GL0 bead in the headgroup region. Normalizing by the number of frames and copy number of each lipid type produces the mean number of lipids of each type around a lipid of a given type; Comparing this value against the probability derived from random chance with no interactions given by the system composition, we obtain the deviation from random chance.

Using smaller systems of approximately 15 by 15 nm in length we computed the lateral pressure profiles for each composition. Each small system was equilibrated for 4 μ s followed by 200 ns of production with positions and velocities written out every 5 ps in full numerical precision. The stresses for each frame by reprocessing using gmx-ls in gromacs 2016.3 (Vanegas *et al*, 2014). Contours for stress calculation were spaced approximately 1 nm in the X and Y directions (in-plane of the membrane) and 0.1 nm in the Z direction (normal to the membrane). The lateral pressure, $p(z)$, is given by $p(z) = \sigma_{zz} - (\sigma_{xx} + \sigma_{yy})/2$, where σ_{xx} , σ_{yy} , and σ_{zz} are the diagonal components of the stress tensor. The discrete lateral pressure profile

was fit using a piecewise cubic interpolation and the bending moment, $K_c c_0 = \int_0^{\infty} zp(z)dz$, was evaluated using numerical integration of the interpolated function. Errors of values derived from and the lateral pressure profile were estimated by splitting the collected production frames into three non-overlapping chunks.

Continuum modeling of tubular cristae formation

Background: In the Helfrich-Canham-Evans model (Helfrich, 1973; Canham, 1970; Evans, 1973), membranes are treated as a two-dimensional surface with an elastic bending energy given by:

$$E = \int_{\Omega} (\kappa_c (H - C_0)^2 + \kappa_G K) dA + \lambda dA.$$

where κ_c is the bending modulus of the membrane (stiffness), H is the mean curvature of the structure, C_0 is the net spontaneous curvature across the bilayer, κ_G is the Gaussian modulus, K is the Gaussian curvature, and λ is the membrane tension. The total energy of the membrane (E) is obtained by integrating the energy density of the manifold over the area Ω . When this energy is minimized, the shape of the membrane corresponding to mechanical equilibrium is obtained.

Overview of the model: The mathematical derivations of this model can be found in extensive detail in (Mahapatra, 2022). Here, we provide a brief summary of the equations. The membrane is modeled as a thin elastic shell in mechanical equilibrium. Table 1 summarizes the symbols and notation; all nonscalar quantities are denoted by a bar overhead.

Table 1: Notation and list of symbols

| Notation | Description | Unit |
|------------------------------------|---|--------------------|
| W | Free energy density of the membrane | pN/nm |
| κ | Bending modulus of the membrane | pN · nm |
| κ_d | Deviatoric modulus of the membrane | pN · nm |
| \bar{n} | Surface normal | 1 |
| $a_{\alpha\beta}, a^{\alpha\beta}$ | Metric tensor and its contravariant | – |
| $b_{\alpha\beta}, b^{\alpha\beta}$ | Curvature tensor and its contravariant | – |
| \bar{T} | Surface traction | pN/nm |
| s | Arclength along the membrane | nm |
| ψ | Angle made by surface tangent with the horizontal direction | 1 |
| H | Mean curvature | nm ⁻¹ |
| D | Deviatoric curvature | nm ⁻¹ |
| C_0 | Spontaneous mean curvature | nm ⁻¹ |
| D_0 | Spontaneous deviatoric curvature | nm ⁻¹ |
| f^α | Tangential component of the force per unit area | pN/nm ² |
| f_n | Normal component of the force per unit area | pN/nm ² |
| λ | Membrane tension | pN/nm |
| λ_0 | Tension at boundary | pN/nm |
| F_n | Traction at the boundary | pN/nm |

The force balance on the membrane is given by

$$\bar{T}_{;\alpha}^\alpha + p\bar{n} + \bar{f} = 0 \quad (\text{S1})$$

where, $\bar{f} = f^\alpha \bar{a}_\alpha + f_n \bar{n}$ is the external force density applied to the membrane, p is normal pressure on the membrane and \bar{T} is traction on the membrane and given by,

$$\bar{T}^\alpha = N^{\beta\alpha} \bar{a}_\beta + S^\alpha \bar{n} \quad (\text{S2})$$

Here, \bar{N} in-plane components of the stress and is given by

$$N^{\beta\alpha} = \zeta^{\beta\alpha} + b_\mu^\beta M^{\mu\alpha} \text{ and } S^\alpha = -M^{\alpha\beta}_{;\beta} \quad (\text{S3})$$

where, $\zeta^{\beta\alpha}$ and $M^{\beta\alpha}$ are obtained from the following constitutive relationships (Steigmann, 2018)

$$\zeta^{\beta\alpha} = \rho \left(\frac{\partial F}{\partial a_{\alpha\beta}} + \frac{\partial F}{\partial a_{\beta\alpha}} \right) \text{ and } M^{\beta\alpha} = \rho \left(\frac{\partial F}{\partial b_{\alpha\beta}} + \frac{\partial F}{\partial b_{\beta\alpha}} \right), \quad (\text{S4})$$

with $F = W/\rho$ is the energy mass density of the membrane. Combining these we get the balance equations in tangential and normal direction

$$N^{\beta\alpha} - S^\alpha b^\beta_\alpha + f^\alpha = 0, \quad S^\alpha_{;\alpha} + N^{\beta\alpha} b_{\beta\alpha} + p + f_n = 0 \quad (\text{S5})$$

Here f^α and f_n are the tangential and normal components of external force applied to the membrane per unit area.

The energy density of the membrane W is taken as follows to account for the mean and the deviatoric curvature

$$W = \kappa(H - C_0)^2 + \kappa_d(D - D_0)^2. \quad (\text{S6})$$

To obtain tubular shapes, recasting the Helfrich energy in terms of the isotropic spontaneous curvature C_0 and the anisotropic spontaneous curvature D_0 , is a commonly used approach (Kralj-Iglić *et al*, 2020; Kabaso *et al*, 2012; Mahapatra, 2022; Noguchi *et al*, 2022). In this case, the energy is written in terms of the mean curvature and the deviatoric curvature D . The deviatoric curvature is defined as half of the difference between the two principal curvatures.

The tangential force balance relation in Equation (S5), simplifies as

$$\lambda' = 2\kappa(H - C_0) C' + 2\kappa_d(D - D_0) D'_0 - f^s. \quad (\text{S7})$$

The normal force balance relation S5_{||} (the shape equation) becomes

$$p = \frac{L'}{r} + W_H(2H^2 - K) - 2H(W + \lambda - W_D D) - f_n, \quad (\text{S8})$$

where L relates to the expression of the traction, given by

$$\frac{L}{r} = \frac{1}{2}(W_H' - W_D') - \frac{\cos \psi}{r} W_D = -F_n. \quad (\text{S9})$$

where F_n is the traction acting normal to the membrane. The above relation gives a natural boundary condition for L at both the boundaries. At the center, it directly correlates with the value of pulling force as

$$p_f = \lim_{r \rightarrow 0} 2\pi r F_n = -2\pi L(0). \quad (\text{S10})$$

Area parameterization: The governing equations are solved in a patch of the membrane with fixed surface area, where the coat area of protein is prescribed. The arclength parametrization poses some difficulties since the total arclength varies depending on the equilibrium shape of the membrane. Therefore, we did a coordinate transformation of arclength to a local area a as given by

$$\frac{\partial}{\partial s} = 2\pi r \frac{\partial}{\partial a} \quad (\text{S11})$$

Note that in the differential form, local area relates as $da = 2\pi r ds$

The tangential force balance relation in Equation S7 transforms to

$$\frac{\partial \lambda}{\partial a} = 2\kappa(H - C_0) \frac{\partial C_0}{\partial a} + 2\kappa_d(D - D_0) \frac{\partial D_0}{\partial a} - \frac{f^s}{2\pi r}. \quad (\text{S12})$$

The normal force balance relation in Equation S8 becomes

$$p = 2\pi \frac{\partial L}{\partial a} + 2\kappa(H - C_0)(2H^2 - K) - 2H(W + \lambda - 2\kappa_d D(D - D_0)) - f_n \quad (\text{S13})$$

where

$$\frac{L}{r} = \frac{\partial}{\partial a}(\kappa(H - C_0) - \kappa_d(D - D_0)) - \kappa_d(D - D_0) \frac{\cos \psi}{r}. \quad (\text{S14})$$

Numerical methods: We solved the system of equations (Equation S11 to Equation S14) numerically to get the equilibrium shape of the membrane for a coat of protein at the center of an axisymmetric area patch. The solution domain is presented in Figure S6A, along with the input protein coat and the boundary conditions shown in Figure S6A. The protein coat includes both the spontaneous mean curvature cap and a combination of mean and deviatoric spontaneous curvature in the rest of the coat region (Figure S6B). Note that we introduced a shape variable ψ , which denotes the angle made by the tangent from its radial plane. The membrane is clamped at the domain boundary, where both the displacement and the angle $\psi = 0$. The membrane tension is also prescribed at the boundary. At the pole, ψ is taken to be zero, which indicates the smoothness at the center of the membrane. L is set to zero, indicating that there is no pulling force acting at the center.

To solve the system of equations, we used MATLAB-based `bvp4c`, a finite difference-based ODE solver with fourth-order accuracy (MATLAB codes are available https://github.com/Rangamani-ab/arijit_deviatoric_tube.2022). We used a nonuniform grid ranging from 1000 to 10000 points, with the finer grid towards the center. We used a large domain size of 10^6 nm^2 to avoid boundary effects but we show the results focusing on the membrane deformation (region enclosed by the dashed line in Figure S6C). The values of the different parameters used are given in the table below.

List of parameters used in the simulations

| Notation | Description | Range |
|-----------------------|----------------------------------|----------------------------------|
| C_0 | Spontaneous mean curvature | 0.01–0.035 nm^{-1} |
| D_0 | Spontaneous deviatoric curvature | 0–0.035 nm^{-1} |
| $\kappa = (\kappa_d)$ | Bending modulus of the membrane | 10-20 $k_B T$ |
| a_{coat} | Coat area of protein | $1.413 \times 10^4 \text{ nm}^2$ |
| a_{mem} | Total area of the membrane | $5.65 \times 10^5 \text{ nm}^2$ |
| λ_0 | Tension at boundary | 0.01 pN/nm |

Parameter ranges: The parameter ranges for the continuum model were chosen from the literature and from the CGMD simulations. The range of anisotropic spontaneous curvature induced by the ATP synthases was estimated from the CGMD simulations presented in (Anselmi *et al*, 2018) for a single ATP synthase dimer by estimating the two principal curvatures for the small deformation seen in Figure 1 of that work. Note that these estimates are obtained from digitizing the images and do not contain the information carried in the thermal fluctuations. The bending moduli range was in the range consistent with CG-MD calculations and previous experimental measurements. The tension and the coat area are free parameters in the model and were tuned such that we could obtain tubules of length and radius consistent with experimental measurements as shown in Figure 5B.

References

- Abraham MJ, Murtola T, Schulz R, Páll S, Smith JC, Hess B & Lindahl E (2015) GROMACS: High performance molecular simulations through multi-level parallelism from laptops to supercomputers. *SoftwareX* 1-2: 19–25
- Acehan D, Malhotra A, Xu Y, Ren M, Stokes DL & Schlame M (2011) Cardiolipin affects the supramolecular organization of ATP synthase in mitochondria. *Biophys J* 100: 2184–2192
- Anselmi C, Davies KM & Faraldo-Gómez JD (2018) Mitochondrial ATP synthase dimers spontaneously associate due to a long-range membrane-induced force. *J Gen Physiol*: jgp.201812033
- Bauer P, Hess B & Lindahl E (2022) GROMACS 2022.1 Source code
- Berendsen HJC, Postma JPM, van Gunsteren WF, DiNola A & Haak JR (1984) Molecular dynamics with coupling to an external bath. *J Chem Phys* 81: 3684–3690
- Bertram R, Gram Pedersen M, Luciani DS & Sherman A (2006) A simplified model for mitochondrial ATP production. *J Theor Biol* 243: 575–586
- Brown FLH (2008) Elastic modeling of biomembranes and lipid bilayers. *Annu Rev Phys Chem* 59: 685–712
- Bussi G, Donadio D & Parrinello M (2007) Canonical sampling through velocity rescaling. *J Chem Phys* 126: 014101
- Canham PB (1970) The minimum energy of bending as a possible explanation of the biconcave shape of the human red blood cell. *J Theor Biol* 26: 61–81
- Davies KM, Anselmi C, Wittig I, Faraldo-Gómez JD & Kühlbrandt W (2012) Structure of the yeast F₁F_o-ATP synthase dimer and its role in shaping the mitochondrial cristae. *Proc Natl Acad Sci U S A* 109: 13602–13607
- De Pinto V, Ludwig O, Krause J, Benz R & Palmieri F (1987) Porin pores of mitochondrial outer membranes from high and low eukaryotic cells: biochemical and biophysical characterization. *Biochim Biophys Acta* 894: 109–119
- E. B-O (2021) MDAnalysis Membrane Curvature Tool
- Ergüder MF & Deserno M (2021) Identifying systematic errors in a power spectral analysis of simulated lipid membranes. *J Chem Phys* 154: 214103
- Evans EA (1973) A new material concept for the red cell membrane. *Biophys J* 13: 926–940
- Forman NG & Wilson DF (1983) Dependence of mitochondrial oxidative phosphorylation on activity of the adenine nucleotide translocase. *J Biol Chem* 258: 8649–8655
- Fowler PW, Hélie J, Duncan A, Chavent M, Koldsø H & Sansom MSP (2016) Membrane stiffness

- is modified by integral membrane proteins. *Soft Matter* 12: 7792–7803
- Frewein MPK, Rumetshofer M & Pabst G (2019) Global small-angle scattering data analysis of inverted hexagonal phases. *J Appl Crystallogr* 52: 403–414
- Garcia GC, Bartol TM, Phan S, Bushong EA, Perkins G, Sejnowski TJ, Ellisman MH & Skupin A (2019) Mitochondrial morphology provides a mechanism for energy buffering at synapses. *Sci Rep* 9: 18306
- Garcia GC, Bartol TM & Sejnowski TJ (2022) A Thermodynamically-Consistent Model for ATP Production in Mitochondria. *bioRxiv*: 2022.08.16.500715
- Harris CR, Millman KJ, van der Walt SJ, Gommers R, Virtanen P, Cournapeau D, Wieser E, Taylor J, Berg S, Smith NJ, *et al* (2020) Array programming with NumPy. *Nature* 585: 357–362
- Helfrich W (1973) Elastic Properties of Lipid Bilayers: Theory and Possible Experiments. *Zeitschrift für Naturforschung C* 28: 693–703 doi:10.1515/znc-1973-11-1209 [PREPRINT]
- Jablin MS, Akabori K & Nagle JF (2014) Experimental support for tilt-dependent theory of biomembrane mechanics. *Phys Rev Lett* 113: 248102
- de Jong DH, Baoukina S, Ingólfsson HI & Marrink SJ (2016) Martini straight: Boosting performance using a shorter cutoff and GPUs. *Comput Phys Commun* 199: 1–7
- Jo S, Kim T & Im W (2007) Automated builder and database of protein/membrane complexes for molecular dynamics simulations. *PLoS One* 2: e880
- Kabaso D, Bobrovska N, Gozdz W, Gov N, Kralj-Iglic V, Veranic P & Iglic A (2012) On the role of membrane anisotropy and BAR proteins in the stability of tubular membrane structures. *J Biomech* 45: 231–238
- Kaltenegger M, Kremser J, Frewein MPK, Zihel P, Bonthuis DJ & Pabst G (2021) Intrinsic lipid curvatures of mammalian plasma membrane outer leaflet lipids and ceramides. *Biochim Biophys Acta Biomembr* 1863: 183709
- Kerr RA, Bartol TM, Kaminsky B, Dittrich M, Chang J-CJ, Baden SB, Sejnowski TJ & Stiles JR (2008) Fast Monte Carlo Simulation Methods for Biological Reaction-Diffusion Systems in Solution and on Surfaces. *SIAM J Sci Comput* 30: 3126–3149
- Kralj-Iglič V, Pocsfalvi G, Mesarec L, Šuštar V, Hägerstrand H & Iglič A (2020) Minimizing isotropic and deviatoric membrane energy - An unifying formation mechanism of different cellular membrane nanovesicle types. *PLoS One* 15: e0244796
- Kucerka N, Tristram-Nagle S & Nagle JF (2005) Structure of fully hydrated fluid phase lipid bilayers with monounsaturated chains. *J Membr Biol* 208: 193–202
- Kushnirov VV (2000) Rapid and reliable protein extraction from yeast. *Yeast* 16: 857–860
- Magnus G & Keizer J (1997) Minimal model of beta-cell mitochondrial Ca²⁺ handling. *Am J Physiol* 273: C717–33

- Mahapatra A (2022) Formation of protein-mediated tubes is governed by a snapthrough transition. *bioRxiv*: 2022.06.07.494774
- Marrink SJ, Risselada HJ, Yefimov S, Tieleman DP & de Vries AH (2007) The MARTINI force field: coarse grained model for biomolecular simulations. *J Phys Chem B* 111: 7812–7824
- Marrink SJ, de Vries AH & Mark AE (2004) Coarse Grained Model for Semiquantitative Lipid Simulations. *J Phys Chem B* 108: 750–760
- Noguchi H, Tozzi C & Arroyo M (2022) Binding of anisotropic curvature-inducing proteins onto membrane tubes. *arXiv [cond-mat.soft]*
- Parrinello M & Rahman A (1981) Polymorphic transitions in single crystals: A new molecular dynamics method. *J Appl Phys* 52: 7182–7190
- Paumard P, Vaillier J, Couly B, Schaeffer J, Soubannier V, Mueller DM, Brèthes D, di Rago J-P & Velours J (2002) The ATP synthase is involved in generating mitochondrial cristae morphology. *EMBO J* 21: 221–230
- Pietrobon D & Caplan SR (1985) Flow-force relationships for a six-state proton pump model: intrinsic uncoupling, kinetic equivalence of input and output forces, and domain of approximate linearity. *Biochemistry* 24: 5764–5776
- Qi Y, Ingólfsson HI, Cheng X, Lee J, Marrink SJ & Im W (2015) CHARMM-GUI Martini Maker for Coarse-Grained Simulations with the Martini Force Field. *J Chem Theory Comput* 11: 4486–4494
- Rabl R, Soubannier V, Scholz R, Vogel F, Mendl N, Vasiljev-Neumeyer A, Körner C, Jagasia R, Keil T, Baumeister W, *et al* (2009) Formation of cristae and crista junctions in mitochondria depends on antagonism between Fc1 and Su e/g. *J Cell Biol* 185: 1047–1063
- Rak M & Tzagoloff A (2009) F1-dependent translation of mitochondrially encoded Atp6p and Atp8p subunits of yeast ATP synthase. *Proc Natl Acad Sci U S A* 106: 18509–18514
- Rawicz W, Olbrich KC, McIntosh T, Needham D & Evans E (2000) Effect of Chain Length and Unsaturation on Elasticity of Lipid Bilayers. *Biophysical Journal* 79: 328–339
doi:10.1016/s0006-3495(00)76295-3 [PREPRINT]
- Saa A & Siqueira KM (2013) Modeling the ATP production in mitochondria. *Bull Math Biol* 75: 1636–1651
- Steigmann DJ (2018) Mechanics and Physics of Lipid Bilayers. In *The Role of Mechanics in the Study of Lipid Bilayers*, Steigmann DJ (ed) pp 1–61. Cham: Springer International Publishing
- Symons JL, Cho K-J, Chang JT, Du G, Waxham MN, Hancock JF, Levental I & Levental KR (2021) Lipidomic atlas of mammalian cell membranes reveals hierarchical variation induced by culture conditions, subcellular membranes, and cell lineages. *Soft Matter* 17: 288–297
- Vanegas JM, Torres-Sánchez A & Arroyo M (2014) Importance of Force Decomposition for Local Stress Calculations in Biomembrane Molecular Simulations. *J Chem Theory Comput* 10:

691–702

Venable RM, Brown FLH & Pastor RW (2015) Mechanical properties of lipid bilayers from molecular dynamics simulation. *Chem Phys Lipids* 192: 60–74

Virtanen P, Gommers R, Oliphant TE, Haberland M, Reddy T, Cournapeau D, Burovski E, Peterson P, Weckesser W, Bright J, *et al* (2020) SciPy 1.0: fundamental algorithms for scientific computing in Python. *Nat Methods* 17: 261–272

Wassenaar TA, Ingólfsson HI, Böckmann RA, Tieleman DP & Marrink SJ (2015) Computational Lipidomics with insane: A Versatile Tool for Generating Custom Membranes for Molecular Simulations. *J Chem Theory Comput* 11: 2144–2155